ELSEVIER

Contents lists available at ScienceDirect

Quaternary Science Reviews

journal homepage: www.elsevier.com/locate/quascirev



Carbon isotope constraints on glacial Atlantic meridional overturning: Strength vs depth



Juan Muglia ^{a, *}, Andreas Schmittner ^b

- ^a Centro para el Estudio de los Sistemas Marinos, CONICET, 2915 Boulevard Brown, U9120ACD, Puerto Madryn, Argentina
- b College of Earth, Ocean and Atmospheric Sciences, Oregon State University, 104 CEOAS Administration Building, 101 SW 26th St, Corvallis, OR, 97331, USA

ARTICLE INFO

Article history: Received 12 October 2020 Received in revised form 6 February 2021 Accepted 8 February 2021 Available online 26 February 2021

Handling Editor: A. Voelker

Keywords:
Paleoclimate modeling
Global
Circulation
Last glacial maximum

ABSTRACT

Despite its importance for climate and the carbon cycle, the deep ocean circulation during the Last Glacial Maximum (LGM) remains poorly understood. Whereas most studies suggest a shallower Atlantic Meridional Overturning Circulation (AMOC) than at present day, there is disagreement about its transport rate, with estimates ranging from stronger to weaker than today. Older deep ocean radiocarbon ages have been suggested to imply a more sluggish circulation. Here we use a global isotope-enabled ocean-climate model to systematically explore the different effects of AMOC depth and strength on carbon isotope (13 C and radiocarbon) distributions and constraints provided by sediment data. We find that existing data constrain the AMOC depth well, favoring simulations with a shallower-than-present LGM AMOC reaching 2000-2500 m of depth. However, they provide weaker constraints on AMOC strength. Comparisons with two high vertical resolution LGM δ^{13} C profiles suggest LGM AMOC strength between 11 and 18 Sv, but more data are needed to refine this estimate. Contrary to past conjectures, we find radiocarbon age to be only weakly related with deep water transport rates, but strongly dependent on Southern Ocean surface reservoir ages, which are highly correlated with AMOC depth. In addition, upon changes of deep transport rates and/or water mass geometry, variations in modeled δ^{13} C and radiocarbon age are highly correlated, suggesting that they do not act as independent traces for physical ocean processes.

© 2021 Elsevier Ltd. All rights reserved.

1. Introduction

Quantifying the global ocean's meridional overturning circulation (MOC) during glacial periods such as the Last Glacial Maximum (LGM, ~ 21 ky in the past) is an important but unresolved topic in paleoceanography. Changes in circulation rate or geometry may have been involved in the observed decrease in atmospheric CO_2 during glacial periods (Marcott et al., 2014) by increasing carbon storage in the deep ocean (Sigman and Boyle, 2000). Furthermore, an observation-based estimate of the MOC could also serve as an independent test for climate models that are used for future projections (Muglia and Schmittner, 2015). One method to infer the characteristics of physical and biogeochemical processes in past climate states is the use of geotracers, which are measurable quantities that act as indicators of variables of interest. For past ocean conditions, they are typically measured in sea floor sediment

* Corresponding author.

E-mail address: jmuglia@cenpat-conicet.gob.ar (J. Muglia).

cores.

Stable carbon isotope ratios have long been used as tracers of deep ocean water masses: $^{13}C/^{12}C$ (expressed as $\delta^{13}C$ when compared with the ¹³C/¹²C ratio of a standard) measured in shells of the benthic foraminifera genus Cibicidoides traces the contemporaneous ¹³C/¹²C of bottom water dissolved inorganic carbon (DIC), and acts as a proxy for nutrient concentrations, which trace water masses (Duplessy et al., 1988; Heinze et al., 1991; Sarnthein et al., 1994; Curry and Oppo, 2005; Gebbie, 2014). It is also affected by purely biogeochemical processes, such as changes in export production, although these processes can be independently constrained by other tracers such as nitrogen isotopes (e.g., Schmittner and Somes, 2016). On the other hand, $^{14}C/^{12}C$ (radiocarbon), is only minimally affected by biological processes. Due to its production in the atmosphere and radioactive decay, it has been thought of as a tracer for ventilation age and thus flow rates of deep water (Broecker et al., 1990, 2007; Adkins and Boyle, 1997; Sarnthein et al., 2013; Burke et al., 2015; Skinner et al., 2017). However, deep ocean radiocarbon age is also affected by the radiocarbon age

of surface water at high latitudes (preformed radiocarbon age, or surface reservoir age) (Campin et al., 1999; Khatiwala et al., 2012). Due to the different controlling processes of these two deep water tracers, it could be though that they vary independently, and could be combined to constrain both the geometry and transport rates of past deep water masses.

Ocean models that include prognostic equations for the geotracers obtained from sediment samples allow direct model-data comparisons. In some cases this may be used to constrain processes involving variables of interest that are not measured directly for the past ocean. This method has been used with δ^{13} C and radiocarbon age to infer the structure of the Atlantic Meridional Overturning Circulation (AMOC) during the LGM. Most works find that a > 500 m shallower LGM AMOC (compared with preindustrial values) best agrees with carbon isotopes (Tagliabue et al., 2009; Menviel et al., 2017, 2020; Kurahashi-Nakamura et al., 2017; Muglia et al., 2018). However, its strength (i.e., transport rate) during the LGM is still under debate, with model data comparisons that use similar carbon isotope global data compilations but estimate a weaker (Tagliabue et al., 2009; Muglia et al., 2018; Menviel et al., 2020), similar (Menviel et al., 2017), and stronger (Kurahashi-Nakamura et al., 2017) AMOC compared with its preindustrial state.

Recent work that includes multiple tracers suggests that (1) carbon isotopes provide weak constraints on AMOC transport rate and (2) the δ^{18} O contrast across the Florida Strait might be a faithful indicator of glacial AMOC transport (Gu et al., 2020), although current global models used for paleo-climate simulations cannot resolve this feature. However, their study included only two LGM simulations, which questions how general their conclusions are given different possible LGM AMOC configurations. Most previous modeling works that constrained the glacial deep ocean circulation by comparing modeled carbon isotopes with LGM reconstructions used simulation ensembles with varying AMOC strengths. In most of these model ensembles AMOC strength co-varies with AMOC depth (i.e., the vertical reach of the upper cell of the AMOC in the water column), such that simulations with stronger AMOCs exhibit deeper circulations. That is the case for Tagliabue et al. (2009); Menviel et al. (2017); Muglia et al. (2018), and Menviel et al. (2020) who all conclude that a shallow AMOC with weaker than present transport rate best reproduces the isotope data. Kurahashi-Nakamura et al. (2017), however, conclude that a shallow but stronger than present AMOC fits carbon and oxygen isotope data, but their study did not test other configurations such as the shallow and weak AMOC case. As mentioned above, Gu et al. (2020) discriminate between AMOC depth and strength to constrain the AMOC, but their study is limited to only two simulations. Thus, a more systematic exploration of the AMOC depth versus AMOC strength phase space in an isotope-enabled model is desirable.

Recent work in physical oceanography has elucidated the controls of surface forcings on AMOC properties. E.g. Sun et al. (2020) show that AMOC depth is controlled by buoyancy fluxes in the Southern Ocean (SO) and in the North Atlantic. Together with the result from Gu et al. (2020) that the AMOC strength can be modified independently of AMOC depth by changing freshwater fluxes in the North Atlantic, this suggests that AMOC depth and strength are controlled by different forcings and thus are independent properties of the global ocean circulation. However, buoyancy fluxes at high latitudes, especially in the SO, remain poorly known, in part because crucial ice-ocean interactions are not currently represented interactively in most global climate models (Adkins, 2013; Fyke et al., 2018).

Here we run a global coupled circulation-biogeochemical model that includes ¹³C and ¹⁴C carbon isotopes. We produce a wide range of possible LGM circulation scenarios, systematically exploring the

AMOC depth versus strength phase space. Effects of each AMOC property on both isotope distributions are examined and constraints from sediment data are evaluated. The model also includes nitrogen isotopes (¹⁵N), which is used mainly to constrain iron fertilization, but since it is not directly linked to circulation (Somes et al., 2017), it will not be further discussed here. Our goals are to (1) explore effects of AMOC depth and strength on global carbon isotope distributions, (2) test if available global LGM reconstructions of the two carbon isotopes are able to constrain AMOC depth and strength separately, and (3) if the two isotopes respond independently to deep ocean circulations changes and their adequacy to constrain such changes.

2. Methodology

2.1. The model

We use the global climate model of the University of Victoria (UVic) version 2.9 (Weaver et al., 2001), which includes a threedimensional ocean component with 3.6° × 1.8° horizontal resolution and 19 vertical levels governed by the primitive equations, with parameterizations for vertical and isopycnal diffusivity. The model's low resolution does not resolve some important bathymetry features, such as the Florida and Bering Straits, so effects on ocean circulation associated with them are hard to estimate. Some fine scale processes, such as tidal energy dissipation, are parametrized using a prescribed sub-grid bathymetry (Schmittner and Egbert, 2013). Wind fields are prescribed, but a two-dimensional atmospheric model calculates evaporation, precipitation, and air moisture and temperature from thermodynamic equilibrium equations. The low resolution and two dimensional atmospheric model may seem simplistic compared with more complex Earth System Models that include three dimensional atmospheric components (e.g., Braconnot et al., 2012). However, these characteristics allow UVic to produce numerous computationally-efficient simulations and run them for several thousand years to equilibrium including full process-based biogeochemistry and isotopes. UVic includes a dynamic-thermodynamic sea ice model, which accounts for changes in surface salinity due to sea ice melting and forming (Schmittner, 2003). The model is also coupled with a dynamic land vegetation model (Meissner et al., 2003). Its representation of the modern global overturning circulation is mostly consistent with observations (Muglia et al., 2018). However, the model's AMOC is too shallow, by about 500 m in the South Atlantic, where observations indicate a depth of 3500 m (Talley et al., 2003) whereas the model results in a depth of ~ 3000 m. In the North Atlantic at 25 $^\circ$ N this bias is even larger, with the model AMOC depth at \sim 3100 m, whereas the RAPID observations indicate a depth of 4400 m (e.g., Danabasoglu et al., 2014).

UVic is coupled to the Model of Ocean Biogeochemistry and Isotopes (MOBI), which includes interactive cycles for three nutrient species (phosphate, nitrate and iron), oxygen, DIC, particulate organic matter, particulate iron, dissolved organic nitrogen and phosphorous, detritus, zooplankton, regular phytoplankton, diazotrophs (nitrogen fixers), and coccolithophores (Kvale et al., 2015; Muglia et al., 2017).

The MOBI code has been restructured and updated since Muglia et al. (2017). The restructuring, which will be described in more detail elsewhere, has made the code more flexible, readable, and easier to use. One of the major updates is the implementation of prognostic equations for calcifiers (coccolithophores) and calcium carbonate (Kvale et al., 2015). In addition, we have modified some parameters of the biogeochemical model to improve our representation of preindustrial water nutrients, oxygen, and carbon. These changes are listed in Table S1, and the validation of our

preindustrial simulation with a comparison to modern data, shown in Table 1, is similar to the performance of previous versions.

The model has been extensively used to simulate the circulation structure and ocean biogeochemistry of the LGM utilizing as contraints its three prescribed isotopes, which can be compared with past reconstructions. Schmittner and Somes (2016) studied global productivity levels during the LGM, finding that higher productivities are needed in order to reproduce $\delta^{13}C$ and $\delta^{15}N$ LGM reconstructions. Somes et al. (2017) determined possible changes in the nitrogen cycle of the ocean during the LGM. Muglia et al. (2018) constrained SO iron fertilization and deep water mass structure, finding that a combination of enhanced atmospheric iron deposition and reorganization of the deep ocean into a voluminous AABW and a shallow and weak AMOC, compared with the preindustrial state, are needed to reconcile with radiocarbon, δ^{13} C and δ^{15} N LGM reconstructions. Detailed analyses of the state's carbon and oxygen cycles are provided in Khatiwala et al. (2019) and Cliff et al. (2021). However, AMOC depth and strength were correlated in the simulations analyzed by Muglia et al. (2018), which precluded unequivocal attribution of the data fit to either AMOC property and tests of certain combinations such as a strong and shallow AMOC. This caveat of the Muglia et al. (2018) methodology is addressed in the present work.

2.2. LGM simulations

We produce equilibrium LGM simulations that include glacial values for orbital parameters, the ICE6G-C LGM land ice sheet reconstruction (Peltier et al., 2015) as recommended by the protocol of the Paleoclimate Model Intercomparison Phase 4 (PMIP4. Kageyama et al., 2017), and a +1 PSU salinity increase everywhere to account for the lower sea level during the LGM. We apply LGM wind stress fields corresponding to a modern estimate plus anomalies (LGM minus preindustrial) calculated from a multimodel mean of models from the previous phase of PMIP (Braconnot et al., 2012). As seen in Muglia and Schmittner (2015), the most striking feature of this LGM wind stress estimate is a positive anomaly in its eastward component over the North Atlantic caused by the presence of the Laurentide Ice Sheet, which tends to strengthen and deepen the AMOC. Although various works have argued that changes in the Southern Hemisphere Westerlies could have had an important impact on LGM deep circulation (e.g., Toggweiler et al., 2006; Menviel et al., 2017), current, state of the art atmospheric models such as PMIP3 models do not predict significant changes in the SH winds during the LGM and we do not include them in our simulations.

Atmospheric CO₂ levels are set to 189.7 ppm, and the radiative forcing of lower CH₄ and N₂O concentrations is implicitly included. As in Muglia et al. (2018), we include LGM sedimentary and surface iron fluxes, with extra surface SO input to fit LGM δ^{13} C and δ^{15} N

reconstructions.

We vary the model's overturning circulation by adjusting two parameters:

- (1) As in Muglia et al. (2018), we modify the atmospheric model's SH moisture eddy diffusivity to reduce SH meridional moisture transport. Lower SH meridional moisture transport increases SO sea ice cover and salinity through sea ice formation (i.e., brine rejection) and lower precipitation at high southern latitudes, which leads to saltier and more voluminous Antarctic Bottom Water (AABW). This produces a shallower and weaker AMOC (Muglia et al., 2018) (Fig. 1a–c). Diffusivities in our simulations range between 3.39 (default value) and 0.95 × 10⁶ m²/s, and produce SH meridional moisture transport anomalies between 0 and 0.36 Sv (Fig. 1a–c; Fig. S1). Fundamentally, this changes SO buoyancy fluxes, which were most likely influenced by processes that are currently not included in most climate models such as ice-ocean interactions (Adkins, 2013; Fyke et al., 2018).
- (2) Negative surface freshwater flux to the North Atlantic strengthens the AMOC (Fig. 1b), with relatively minor AMOC deepening (Fig. 1d). We apply -0.64, -0.32, -0.16, and -0.08 Sv fluxes to the surface region between $45-65^\circ$ N and $60-0^\circ$ W during the whole duration of the experiments, obtaining different levels of AMOC strengthening. In order to keep global salinity constant a compensating positive fresh water flux is distributed over all other ocean grid boxes.

These forcings are applied as an efficient method to produce different deep circulation geometries and rates. They should not be regarded as realistic representations of LGM forcings but as possibilities given our current lack of understanding and uncertainties as noted in publications such as those cited above. Varying both parameters results in simulations with different combinations of AMOC depth and strength. Simulations without North Atlantic fresh water (i.e., 0 Sv) forcing and default values for SH moisture transport are also included (Table 2, Fig. 1). There exists little constrain from reconstructions on LGM moisture transport (Sigman et al., 2007). The meridional moisture transport multi-model mean from our simulation ensemble is very close to modern observations (Fig. S1). Differences between the observations and individual simulations do not exceed 40 % in the Southern Hemisphere, where the moisture diffusivity anomalies are applied.

Several modeling studies have found that AMOC depth and strength co-vary upon changes in surface forcings with deeper AMOC states being associated to higher transport rates (Nikurashin and Vallis, 2012; Marshall et al., 2017; Sun et al., 2020). In our simulations, AMOC strength and depth are both affected by surface forcings, although AMOC depth does not change as significantly

Table 1
Skill of our preindustrial run to reproduce some key biogeochemical dissolved tracers and isotopes. R corresponds to correlation coefficient and RMSE corresponds to root mean square error normalized by a combination of the model and data standard deviations (SD). SD's are also listed in the table, in units of mmol/m³ for the nutrients and carbon and permil for the isotopes. Note that the carbon isotope observations include anthropogenic effects, which are not considered in the model. This leads to a poor fit of surface values. Data sources: Key et al. (2004) for DIC, Δ^{14} C, Levitus et al. (2013) for PO₄, NO₃, O₂, Schmittner et al. (2013) for δ^{13} C, Schlitzer et al. (2018) for dissolved Fe.

Tracer	R (global)	RMSE (global)	SD (global)	R (surface)	RMSE (surface)	SD (surface)
PO ₄	0.94	0.26	0.89	0.86	0.41	0.74
NO_3	0.93	0.33	13.06	0.92	0.32	10.75
Dissolved Fe	0.39	1.00	0.0005	0.39	0.86	0.0005
O_2	0.93	0.29	87	0.97	0.20	70
DIC	0.95	0.27	120	0.88	0.41	120
δ^{13} C	0.77	0.55	0.77	0.24	2.02	0.44
$\Delta^{14}C$	0.95	0.22	68.24	0.84	0.42	27.01

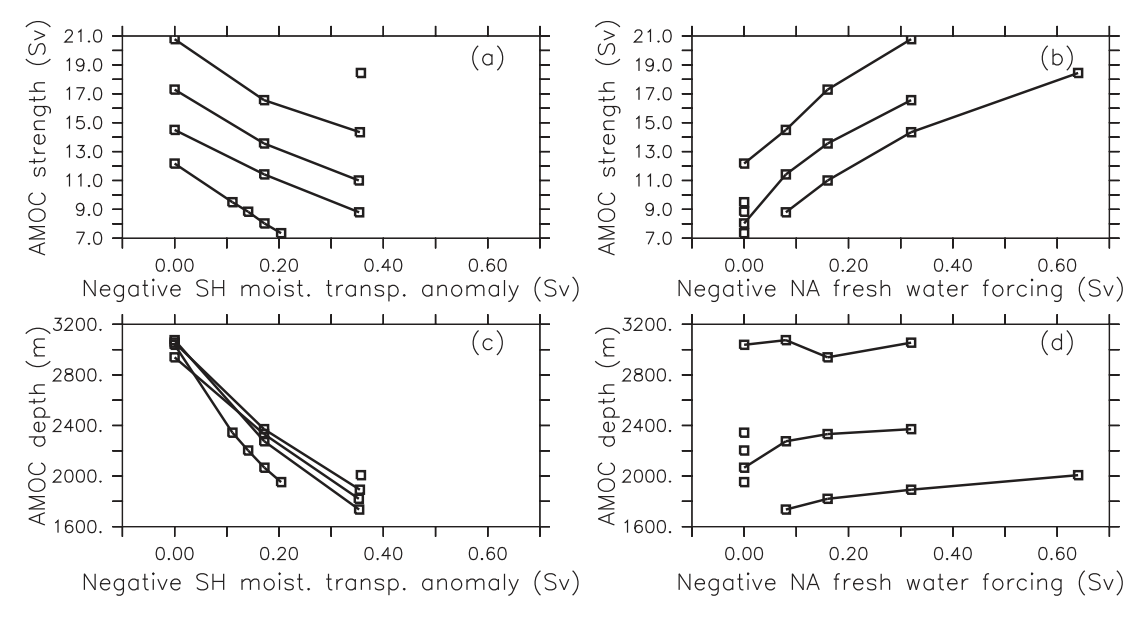


Fig. 1. Effect of the two forcings applied in our LGM simulations on AMOC depth and strength, as indicated. Each square represents a simulation. Simulations that are connected by lines differ only on their (a-c) SH moisture transport or (b-d) NA negative fresh water forcings, and help distinguish the individual effect of each parameter change in our two AMOC metrics. The SH moisture transport anomalies are calculated relative to the simulations with no anomalies applied.

Table 2 Maximum Southern Hemisphere meridional moisture diffusivity $(10^6 \text{ m}^2/\text{s})$ and North Atlantic fresh water forcing (Sv) used in each of our LGM experiments. Experiment names are given by their AMOC strength (in Sv) and depth (in km). The last column lists a description of the type of AMOC of each experiment.

Experiment	SH diff. (10 ⁶ m ² /s)	FWF (Sv)	AMOC type
7.3_1.9	1.89	0	Weak-Shallow
8.0_2.1	2.08	0	Weak-Shallow
8.8_2.2	2.30	0	Weak-Shallow
9.5_2.3	2.52	0	Weak-Shallow
12.2_3.0	3.39	0	Deep
14.5_3.1	3.39	-0.08	Deep
17.3_2.9	3.39	-0.16	Deep
20.8_3.1	3.39	-0.32	Deep
11.4_2.3	2.08	-0.08	Intermediate-Shallow
13.6_2.3	2.08	-0.16	Intermediate-Shallow
16.6_2.4	2.08	-0.32	Intermediate-Shallow
8.8_1.7	0.95	-0.08	Weak-Shallow
11.0_1.8	0.95	-0.16	Intermediate-Shallow
14.3_1.9	0.95	-0.32	Intermediate-Shallow
18.4_2.0	0.95	-0.64	Strong-Shallow

upon changes in North Atlantic fresh water fluxes as with changes in SH moisture fluxes (Fig. 1). On the other hand, results from LGM experiments in PMIP4 (Kageyama et al., 2020), which apply similar boundary conditions to our simulations in terms of ice sheets, green house gases and orbital parameters, exhibit in four of six model cases higher AMOC transport but no considerable change in AMOC depth between LGM and preindustrial experiments. The other two models from that intercomparison present in one case a stronger and deeper LGM AMOC, and in another a shallower and weaker LGM AMOC, when compared with the respective preindustrial experiments. Our LGM experiments are all in the range of these state-of-the-art simulations. Our ensemble of LGM AMOC states is as diverse as possible, to test if the different past AMOC features can be independently constrained by carbon isotopes, but we do not make any assumptions on the feasibility of each configuration in the real ocean.

We include 15 LGM simulations in this work. Each was run for 5000 y, and results shown correspond to an average of the last

500 y, when all tracers were in equilibrium. Fig. 2 shows most of the AMOC streamfunctions produced by our LGM simulations, along with a preindustrial control plot. Panels include simulation names, given by their AMOC strength-depth pairs (in Sv and km). Table 2 lists the forcings applied to each simulation, their names and the general characteristics of their AMOCs. The different experiments are referred to in the following by their AMOC strength in Sv (X) and AMOC depth in km (Y) numbers separated by an underscore X_Y. E.g. experiment 14.5_3.1 refers to the model with an AMOC strength of 14.5 Sv and an AMOC depth of 3.1 km. AMOC strength, defined as the maximum AMOC transport at 25° N, ranges between 8 and 20 Sv. This latitude was chosen because it is close to the latitude of modern observations of AMOC transport (McCarthy et al., 2015). AMOC depth, defined as the average depth of the boundary between the upper and lower cells of the AMOC between 25°S and 25°N, ranges between 1700 and 3100 m. The preindustrial simulation has an AMOC strength of 17.1 Sv and depth of 2900 m. Whereas its strength is consistent with observations its depth is too shallow as discussed above.

Compared to the preindustrial, the LGM simulations display different combinations of strong, weak, shallow, and deep AMOC states, accompanied by different levels of AABW entrainment. The transport of the model's Gulf Stream at 25° N in the preindustrial simulation is 40 Sv. LGM simulations exhibit transports of 40 - 56Sv, and transport increases in simulations with higher AMOC depth and/or strength. The coarse resolution of the model does not resolve bathymetry features that channel this current such as the Florida Strait, so it is hard to make direct comparisons with LGM flow estimates from δ^{18} O profiles such as Lynch-Stieglitz et al. (1999). These estimates predict a weaker Gulf Stream transport across the Florida Strait in the LGM, which seems in disagreement with our model results. The reason is the LGM wind stress estimate used in our LGM simulations, which is very strong over the North Atlantic ocean, and enhances the mid-latitude gyre circulation and northward salt transport associated with the Gulf Stream, as described in Muglia and Schmittner (2015).

Indo-Pacific streamfunctions show less striking differences among simulations (Fig. S2). LGM simulations with a weaker AMOC

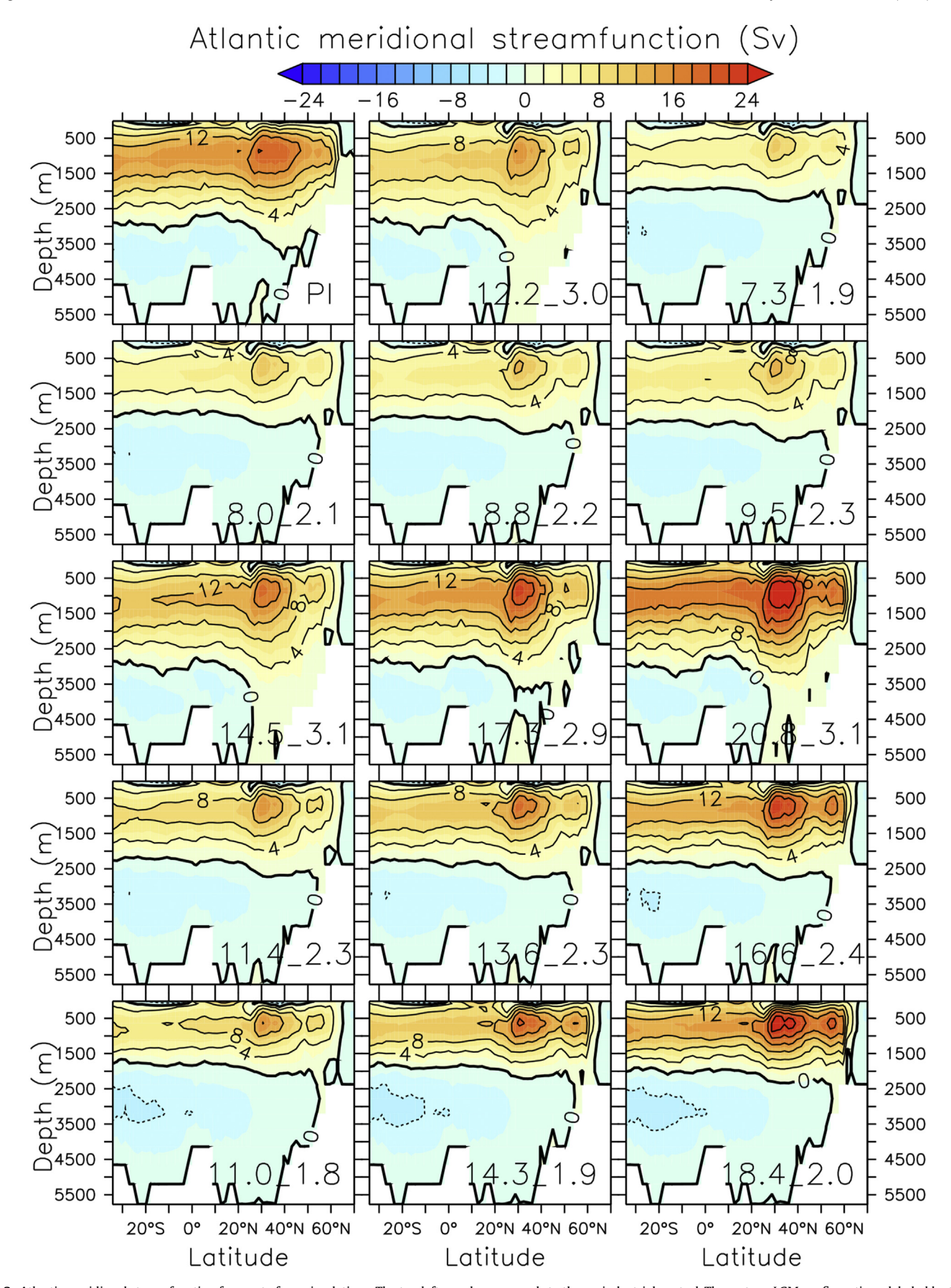


Fig. 2. Atlantic meridional streamfunction for most of our simulations. The top left panel corresponds to the preindustrial control. The rest are LGM configurations, labeled by their AMOC strength-depth (in Sv and km).

(e.g. 14.5_3.1 vs 20.8_3.1 or 7.3_1.9 vs 14.3_1.9) have a higher southward penetration of North Pacific Intermediate Water, reduced inflow of Circumpolar Deep Water and less upwelling at low latitudes.

AMOC shoaling (e.g. $14.3_{-}1.9$ vs $14.5_{-}3.1$) can lead to differences in the in and out flow at 35° S and even flow reversal. E.g. in Fig. 2, whereas model $14.5_{-}3.1$ has inflow below 2000 m and outflow between 1000 and 2000 m, model $14.3_{-}1.9$ has inflow below 3000 m, outflow between 3000 and 2000 m, and inflow again around 1000 m depth, suggesting a separation between deeper SO-sourced inflow and shallower NADW inflow in the shallow AMOC case.

The salinity fields of both the Atlantic and Indo-Pacific oceans are greatly affected by the different deep circulation patterns. In the Atlantic, deep circulation simulations exhibit a pattern similar to the preindustrial, with saltier North Atlantic Deep Water (NADW) than AABW. Simulations that have AMOCs shallower than 3000 m show a pattern more in line with LGM salinity estimates from pore water (Adkins et al., 2002; Insua et al., 2014), with saltier AABW than NADW, and the former occupying a bigger portion of the deep ocean than in present times (Fig. S3). In addition, stronger AMOC simulations produce a more voluminous and fresher Antarctic Intermediate Water (AAIW). In the Indo-Pacific Ocean (Fig. S4), salinity stratification increases for all LGM simulations. Deep AMOC runs produce higher entrainment of salty, Atlantic-sourced waters into the Indo-Pacific. Shallow AMOC runs produce a salty and voluminous AABW, which also affects deep Indo-Pacific salinities increasing its stratification. On the other hand, AMOC strength does not affect the salinities of this basin significantly.

It has been hypothesized that a loss of buoyancy (Ferrari et al., 2014) or an increase in salinity (Sun et al., 2020) of waters around Antarctica may have isolated Antarctic-sourced waters and shallowed the AMOC. Although we do not test this in a direct manner, the effect of decreasing SH moisture transport in our simulations causes these two effects through a decrease in precipitation at high latitudes and an increase in SO sea ice formation and brine rejection (Muglia et al., 2018). Other processes governing deep water formation, such as SO meso-scale eddies (Nikurashin and Vallis, 2012), are not included in the model and remain an import caveat of our methodology, especially affecting AABW formation.

Simulated δ^{13} C and radiocarbon ages from the experiments are compared with LGM reconstructions. The combination of these two tracers has been previously used to constrain deep circulation characteristics in model simulations (Tagliabue et al., 2009; Menviel et al., 2017; Muglia et al., 2018). We have updated previous compilations (Peterson et al., 2014; Skinner et al., 2017) with new data (Tables S2, S3) for a total of 516 and 266 data points for LGM δ^{13} C and radiocarbon age, respectively. Figs. S5 and S6 show the positions and depths of all reconstructions in the compilations.

3. Results

When compared with LGM δ^{13} C reconstructions from the global ocean, our model simulations display correlation coefficients (R) that range between 0.65 and 0.80 (Fig. 3; Table S4). Global root-mean-square errors (RMSE, normalized by the data-model uncertainty (Muglia et al., 2018)) range between 1.1 and 2.2. The skill of each experiment to reproduce the LGM data depends strongly on AMOC depth (Fig. 3). Realizations with an AMOC depth of 2000–2500 m reproduce the data best, with R higher than 0.76 and RMSE lower than 1.3. Realizations with shallower or deeper AMOCs have a worse agreement with the data, especially in the deeper cases. The global model-data agreement versus AMOC depth relation follows the Atlantic signal, indicating the relevance of the AMOC in determining global δ^{13} C distribution (Fig. 3, middle panels) and

reflecting the larger amount of data from the Atlantic. The Indo-Pacific displays less differences in terms of R among simulations than the Atlantic, with higher values for the shallow and weak AMOC cases, and generally good agreement with the data in terms of RMSE (Fig. 3, bottom panels).

The relation of δ^{13} C model-data agreement with AMOC strength is weaker than with AMOC depth as indicated by the mostly horizontal isolines in the upper panels of Fig. 3. Although experiments with weak transport have a slightly better skill at reproducing the data, the difference in R and RMSE among different experiments with similar AMOC depths is much smaller than when comparing skill versus depth (compare the color range of Fig. 3 along the horizontal and vertical axes).

On a regional level, we compare LGM δ^{13} C from our simulations with data at high vertical resolution from the Brazil margin (Hoffman and Lund, 2012; Tessin and Lund, 2013; Lund et al., 2015) (Fig. 4, left; Table S5). Deep AMOC states, reminiscent of many PMIP3 models (Muglia and Schmittner, 2015), are clearly inconsistent with the data as they overestimate $\delta^{13}C$ values below \sim 2000 m depth. Shallow AMOC experiments are able to capture most of the features of the reconstructed vertical profile, including relatively high values of NADW between 1500 and 2000 m depth and decreasing values towards the bottom. However, the sediment data show a pronounced minimum for AAIW around 1100 m depth above the maximum for NADW. This feature of increasing δ^{13} C with depth between 1100 and 1500 m is not reproduced by shallow and weak AMOC simulations. Shallow and weak AMOC simulations also underestimate the δ^{13} C maximum between 1500 and 2000 m. Shallow-intermediate/strong AMOC states (11 - 18 Sv), on the other hand, reproduce these features better. Quantitatively, shallow-intermediate/strong AMOC simulations provide the best model-data agreement, with R ranging between 0.83 and 0.90 and RMSE (not normalized) ranging between 0.22 and 0.29 permil, compared with 0.79 - 0.83 and 0.29 - 0.35 permil for shallowweak AMOC simulations, and 0.53 - 0.67 and 0.43 - 0.59 permil for deep AMOC simulations. A similar result is found for data of high vertical resolution from the southwest Pacific (Sikes et al., 2016) (Fig. 4, right). RMSE for shallow, strong AMOC simulations range between 0.16 and 0.24 permil, compared with 0.23-0.30 for both shallow-weak and deep AMOC cases (Table S5).

Models with a shallower AMOC display older global-mean radiocarbon ages (Fig. 5a; Table S6), whereas AMOC strength, perhaps surprisingly, does not affect whole-ocean radiocarbon age much. The difference between model and reconstructed mean radiocarbon age, calculated only in grid boxes where data exist, shows values closer to zero (indicating model-data agreement) in the shallow AMOC cases, but only minor sensitivity to AMOC strength such that stronger AMOC states at the same AMOC depth produce slightly younger radiocarbon ages. Experiments with AMOC depths between 2000 and 2500 m have the lowest bias, and underestimate the reconstructed global radiocarbon age by only $10 - 80^{14}$ C y. Experiments with shallower AMOC depths than that range overestimate the reconstructions by $50 - 100^{-14}$ C y, and the ones with deeper AMOC underestimate them by $\sim 200^{14}$ C y. Note, however, that the mean radiocarbon age estimate from the data may depend on subjective decisions such as the removal of outliers (e.g. Skinner et al. (2017) removed all data with ages larger than 6000 ¹⁴C y).

Simulations with a shallow AMOC have the best performance compared against LGM data from the Atlantic (Fig. 6). A single very strong and deep AMOC case (simulation 20.8_3.1 in Table 2) also shows good agreement with the Atlantic data, although its high bias in global radiocarbon age (Fig. 5a) and inconsistency with δ^{13} C

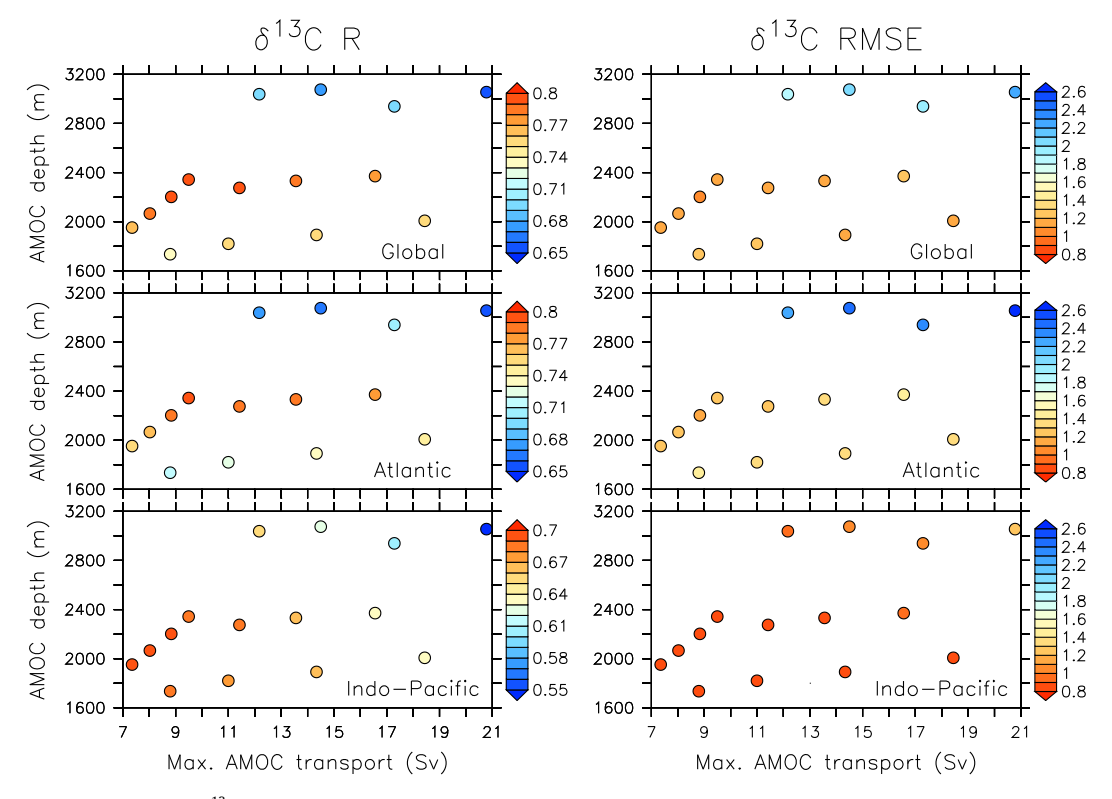


Fig. 3. Metrics of model-data agreement of δ^{13} C of dissolved inorganic carbon (DIC) from our LGM simulations compared with LGM reconstructions, organized in AMOC strength-depth plots. The color scale corresponds to (left plots) correlation coefficient (R) or (right plots) root mean square error (RMSE). RMSE's are normalized by the combination of preindustrial model and data uncertainties, which we estimate as 0.30 permil. Contours were calculated by interpolation. Note that the color scale for the Indo-Pacific R has different limits than for the other two R plots. ('erpretation of the references to color in this figure legend, the reader is referred to the Web version of this article.)

data (Fig. 3) deem it as an unlikely LGM scenario. In the global ocean, simulations with AMOC depths between 2200 and 2400 m and strengths higher than 10 Sv exhibit the lowest RMSE, but there is little distinction in the performance of each simulation in terms of R (Fig. 6; Table S6). The radiocarbon age model-data agreement signal does not follow the Atlantic pattern as close as in the case of δ^{13} C, possibly due to a greater number of LGM radiocarbon data points in the Indo-Pacific than in the Atlantic. As for δ^{13} C, the isolines for R and RMSE for radiocarbon are also mostly horizontal in Fig. 6, indicating better constraints on AMOC depth than on AMOC strength.

4. Discussion

 δ^{13} C from benthic foraminifera shell samples has been identified as a tracer for deep water mass geometry and distribution (Curry and Oppo, 2005; Gebbie, 2014). On the other hand, the difference between benthic and atmospheric radiocarbon age, which can be obtained from benthic and planktonic foraminifera samples combined with estimates of surface reservoir age (Butzin et al., 2017), has been interpreted as an indicator of deep water ventilation age (Sarnthein et al., 2013; Davies-Walczak et al., 2014; Skinner et al., 2017), which is often used synonymously with circulation rate. However, the radiocarbon-age versus ventilation (ideal) age relation is complicated by the fact that radiocarbon age is not only affected by the time since a water parcel was in contact with the atmosphere, but also by its surface (or preformed) value at high latitude sites of deep water formation, which is advected into the ocean's deep interior (Campin et al., 1999; Khatiwala et al., 2012).

Here, water mass geometry, reflected in AMOC depth, is the

dominant factor in determining the model's ability to reproduce LGM δ^{13} C and radiocarbon, whereas the AMOC mass transport rate plays only a secondary role. To illustrate those sensitivities we examine the effects of AMOC strengthening and AMOC deepening on both carbon isotope distributions. Fig. 7 shows that a 1200 m AMOC deepening affects deep isotope values more strikingly than a 7 Sv AMOC strengthening.

AMOC strengthening increases Atlantic δ^{13} C between 1000 and 2500 m and in bottom waters because of more southward penetration of isotopically heavy NADW, which also imprints its signal into AABW. The amplitude of these changes is less than 0.2 permil, and thus may be difficult to detect given the uncertainties in δ^{13} C reconstructions, which are typically ~ 0.25 permil (Schmittner et al., 2017). Similar to Schmittner et al. (2007), AMOC strengthening leads to weaker overturning (Fig. 8) and increased stratification in the SO (Fig. S3). Decreased upwelling by the SO MOC and more nutrient-poor NADW being mixed with SO waters lower SO productivity and decrease $\delta^{13}C$ in the upper Pacific and South Atlantic (Fig. 9). This signal is amplified in the subtropics due to increased productivity there owing to increased low latitude upwelling, which leads to more remineralization of low δ^{13} C organic matter in the shallow subsurface ocean there (Fig. S2). Thus, more data from those upper ocean regions, where the data density is currently low, could improve future AMOC strength estimates. δ^{13} C is most sensitive to AMOC strengthening in the Atlantic Ocean above ~ 2500 m between 40° S and 40° N (Fig. 7). The Brazil margin site that we analyze sits inside this region, and if available. more high vertical resolution sites there would have the potential to further constrain AMOC strength. In the Indo-Pacific, maximum sensitivity occurs above 2000 m. However, the comparison with the

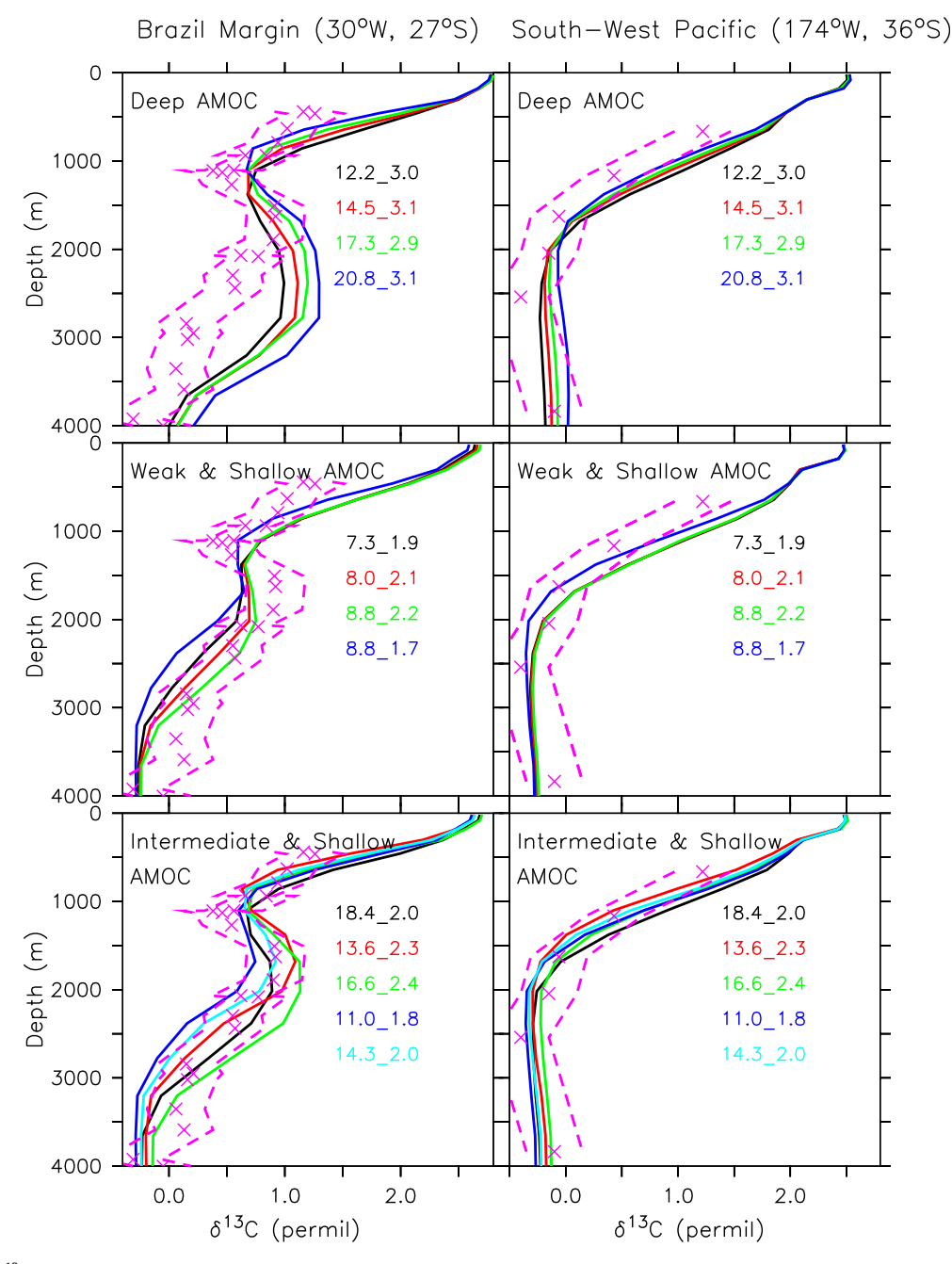


Fig. 4. Comparison of δ^{13} C from our simulations with benthic LGM data of high vertical resolution from (left) the Brazil margin and (right) the South West Pacific. Simulations are grouped in three panels depending on their general AMOC structure, as indicated. Purple symbols indicate the reconstructed values, and purple dashed lines the \pm 0.25 permil uncertainties estimated from Schmittner et al. (2017). Given their overall lower skill to reproduce the data, we group all deep AMOC simulations into one category, regardless of their AMOC strength. (For interpretation of the references to color in this figure legend, the reader is referred to the Web version of this article.)

southwest Pacific data (Fig. 4), which lies outside of this region, suggests that even outside of it, high resolution LGM vertical $\delta^{13} C$ profile reconstructions that are less noisy than a global compilation from multiple sources could be used to constrain the LGM's AMOC strength. Similarly to $\delta^{13} C$, AMOC strengthening leads to a slight decrease ($\sim 100^{-14} C$ y) of radiocarbon ages in most of the deep ocean, because of increased contributions of relatively young NADW.

In contrast to the relatively small changes from AMOC strenghtening, deepening of the AMOC induces a large signal in the deep Atlantic, with δ^{13} C increasing by more than 1 permil and

radiocarbon ages decreasing by more than 700 ^{14}C y. SO export production increases due to strengthening of the SO MOC and enhanced mixing (Fig. 8), similarly to results obtained from productivity proxies south of the Polar Front (Hillenbrand and Cortese (2006); Jaccard et al. (2013)). This induces a high surface $\delta^{13}\text{C}$ signal that gets advected elsewhere (Fig. 9). Even in the deep Indo-Pacific AMOC deepening leads to a much larger reduction in radiocarbon age ($\sim 200^{-14}\text{C}$ y) than AMOC strengthening ($\sim 100^{-14}\text{C}$ y).

The effects of AMOC deepening and strengthening on δ^{13} C and radiocarbon are highly anti-correlated (R < - 0.95, Fig. 7), indicating that they may not be independent tracers of physical

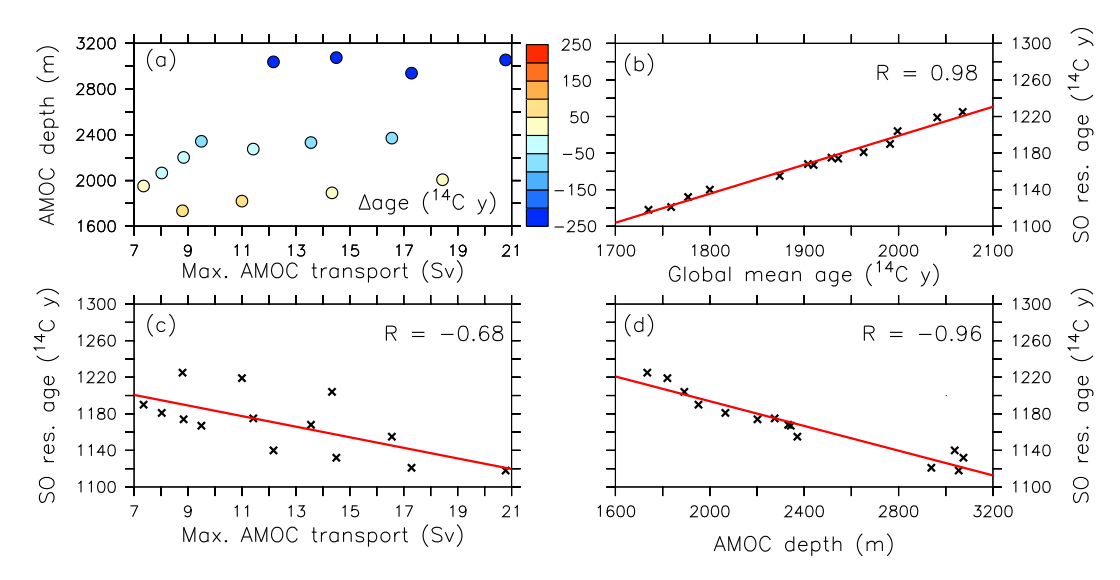


Fig. 5. (a) Model minus data-reconstructed global mean radiocarbon age calculated at grid boxes where there exists data (Δ age). (b) Mean SO surface reservoir age versus global mean age from our simulations. (c–d) SO surface reservoir age as a function of AMOC (c) strength and (d) depth from our simulations. Linear regressions are overlaid in (b–d), with correlation coefficients indicated at each panel.

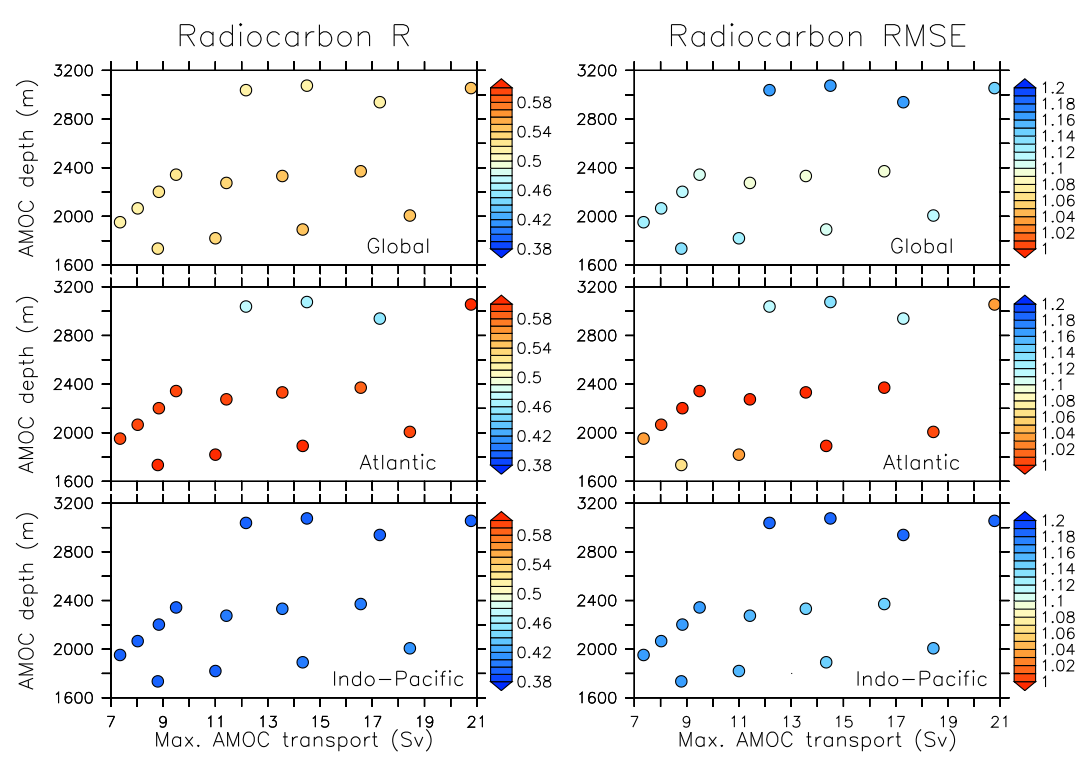


Fig. 6. Same as Fig. 2, but for radiocarbon age. RMSE's are normalized by the combination of preindustrial model and data uncertainties, which we estimate in 65014C y.

processes in the ocean. As an additional test, we calculated the correlation coefficient associated to the differences in $\delta^{13}C$ and radiocarbon age when comparing each of our LGM simulations with 12.2_3.0, which can serve as a default UVic LGM case because it is the simulation with the least amount of "extra" forcings (Table 2). In all cases, correlation coefficient is ~ -0.95 . This is a strong indicator that radiocarbon and $\delta^{13}C$ do not behave as independent tracers for physical processes in the ocean, such as changes in deep circulation or water mass geometry. Their effects are more decoupled when purely biogeochemical processes that affect $\delta^{13}C$

but do not vary radiocarbon significantly come into play, such as an increase in SO export production due to iron fertilization (Muglia et al., 2018). For example, we ran an additional simulation like 12.2_3.0 but with decreased SO surface iron flux as in Muglia et al. (2018); when comparing 12.2_3.0 to this lower iron simulation we find a -0.5 permil decrease on deep $\delta^{13} C$ (Fig. S7), but negligible effects on radiocarbon age, which decrease slightly in deep waters due to an increase in DIC concentrations (not shown).

By an inverse modeling approach, Marchal and Curry (2008) suggest that a maximum uncertainty of 0.1 permil in $\delta^{13}C$

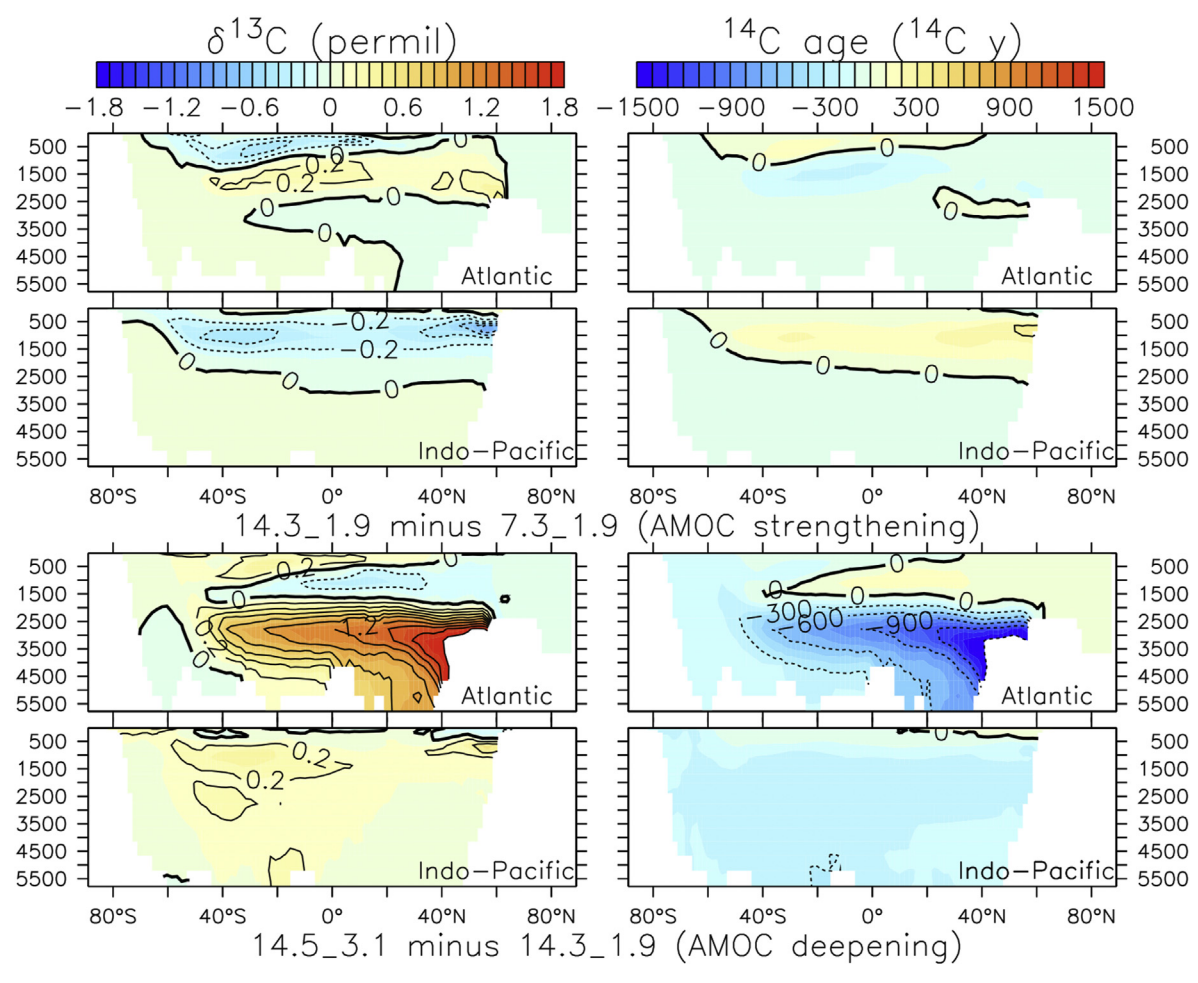


Fig. 7. Effects on δ^{13} C and radiocarbon age of AMOC strengthening and deepening in the Atlantic and Indo-Pacific oceans (zonal means). We use the difference between two pairs of simulations, each pair showing one of the effects, as indicated with the labels from Fig. 2.

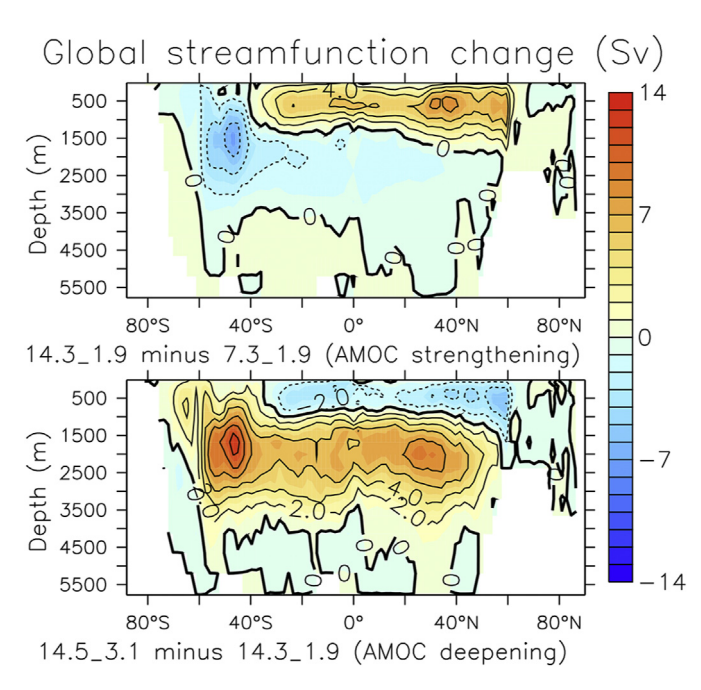


Fig. 8. Differences in global total MOC between the same simulations of Fig. 6.

reconstructions is needed to correctly constrain the LGM deep circulation and distinguish it from the preindutrial state. Another inverse modeling study (Huybers et al., 2007) found that given their current level of uncertainty and sparseness, paleotracers such as δ^{13} C and radiocarbon can potentially be used to estimate past water mass volumes, but not transport rates. The uncertainties of the data used here, calculated from the relationship between δ^{13} C of DIC and of benthic foraminifera (Cibicidoides) from Holocene data are closer to 0.25 permil (Schmittner et al., 2017). However, the RMSE's that we get when comparing our deep AMOC runs' δ^{13} C with the global LGM reconstructions are the highest among the simulations presented here (2.27 - 2.69, Table S4), and almost double the ones obtained with the shallow AMOC LGM simulations (1.10 - 1.20, Table S4). The large differences in RMSE in these two different circulation states may indicate that global compilations of δ^{13} C can be used to constrain the general characteristics of water mass geometry. On a regional level, results from the Brazil margin and southwest Pacific suggest that it may be possible to constrain the AMOC in a more detailed way if the model-data comparison is done at locations with high-resolution vertical profiles of LGM δ^{13} C reconstructions. Although we find intermediate to stronger (11-18 Sv) and shallower (1800-2400 m) AMOC cases among LGM simulations to best agree with these data, there is a high level of uncertainty in the estimated AMOC strength, and more high resolution locations are needed in order to increase the skill of

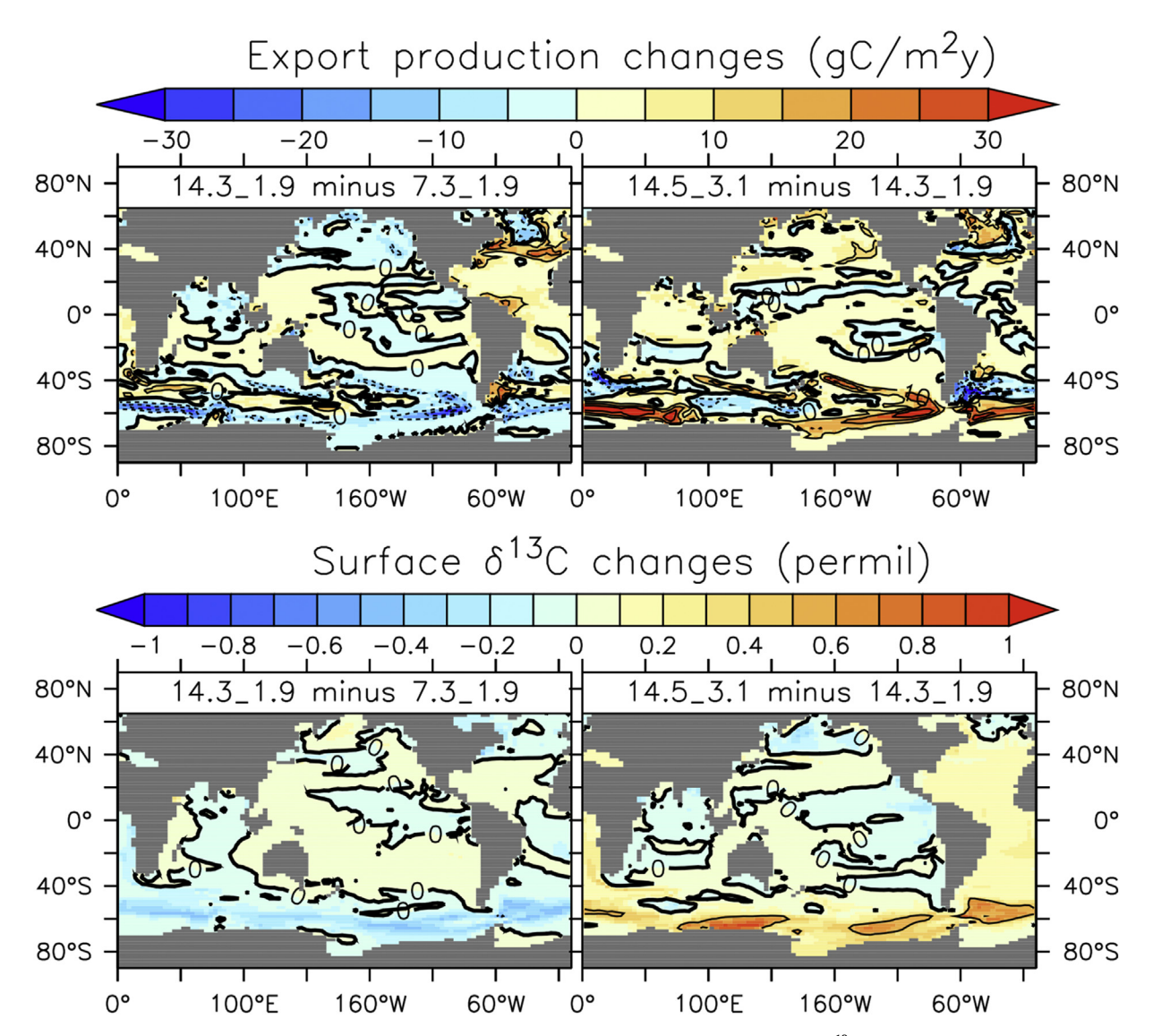


Fig. 9. Effects of AMOC (left) strengthening and (right) deepening on export production out of the euphotic zone and surface δ^{13} C, as indicated. The simulations used are the same as in Fig. 6.

glacial AMOC estimates calculated by this method.

As a proxy for water mass ventilation, radiocarbon age has been linked, in an intuitive manner, to water transport associated with overturning circulation (Skinner et al., 2017). However, Khatiwala et al. (2019) showed that deep radiocarbon ages depend strongly on SO surface reservoir ages, and the results presented here exhibit a very high correlation between global mean radiocarbon ages and mean SO surface reservoir ages (Fig. 5b). In our simulations, mean SO reservoir ages are more closely correlated with AMOC depth than strength (Fig. 5c and d).

Less sinking of dense waters (i.e., more positive buoyancy fluxes) around Antarctica in high meridional moisture flux simulations decrease AABW entrainment into the Atlantic, and deepen the AMOC (Fig. 2), as proposed by Ferrari et al. (2014). SO MOC transport is also enhanced in deep AMOC simulations (Fig. 8), which tends to increase SO surface reservoir ages. However, the effect is overcompensated by the lower SO buoyancy flux, which tends to lower them because of lower sea ice cover (not shown). The result is a strong negative correlation between SO surface reservoir ages and AMOC depth (Fig. 5), which itself is proportional to negative

buoyancy flux around Antarctica (Figs. S8, S9). On the other hand, the direct dependence of AMOC strength with SO buoyancy fluxes is weaker (Fig. S8), and simulations with very different AMOC transports can have similar SO buoyancy fluxes (Fig. S9). This suggests that either radiocarbon age depends strongly on AMOC depth, or they are both affected by SO surface processes set by the applied boundary conditions. As a consequence deep radiocarbon ages are highly correlated with AMOC depth, the level of model-data agreement of each simulation is mainly linked to that AMOC depth (Fig. 6), and AMOC strength is only weakly constrained by radiocarbon age.

The effect on carbon content of the ocean of the different circulation configurations shows a tendency towards higher values at shallower and slower AMOC (Fig. 10). The geometry of the water masses plays an important role, since with a shallower AMOC, carbon-rich AABW occupies a greater portion of the deep ocean, increasing global carbon content (Muglia et al., 2018) (Fig. S10). A decrease in the transport rate of the AMOC produces a similar effect, although of less magnitude than a decrease of its depth (Fig. 10). The quantification of the effect of different physical ocean

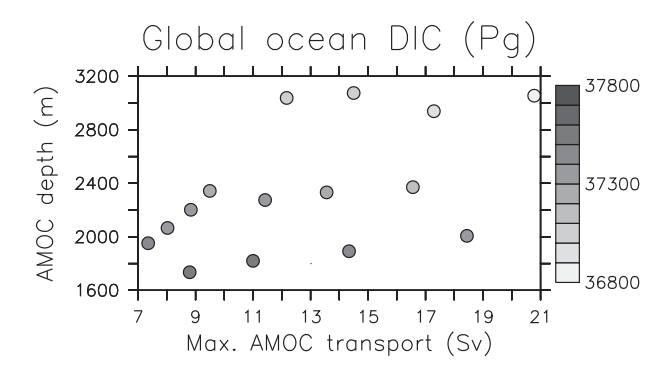


Fig. 10. Globally-integrated DIC from our simulations, organized in an AMOC strengthdepth plot.

configurations on global ocean carbon content is relevant due to the presumption of higher values during the LGM than in the Late Holocene (Sigman et al., 2010), although it has been suggested from ocean models that temperature and biogeochemistry have a bigger effect on ocean carbon content than circulation (Tagliabue et al., 2009; Khatiwala et al., 2019). A detailed carbon cycle analysis of these simulations is beyond the scope of this paper and will be presented elsewhere.

Our simulations suggest that δ^{13} C and radiocarbon from benthic foraminifera samples serve as tracers for water mass geometry, but the rate of transport of the AMOC, an important quantity for climate change (Hofmann and Rahmstorf, 2009; Buizert and Schmittner, 2015), is not well constrained by them. This is in agreement with a recent study that finds δ^{13} C more heavily affected by AMOC depth than strength in the glacial ocean (Gu et al., 2020). The results highlight the need of global circulation models to include prognostic equations for additional, more adequate paleo-tracers of AMOC strength. Our results expand on previous studies with the UVic model on LGM deep circulation. Muglia et al. (2018) found that both biogeochemical and circulation changes are needed to reproduce stable isotope ratios and radiocarbon ages from the deep ocean of the LGM. Here we find that not all aspects of the deep water mass structure can be constrained by those isotopes.

Caveats are associated with the coarse resolution of our model. which may not realistically simulate sharp features such as western boundary currents. Those features may be too broad and diffuse in the model, which may impact comparisons to sediment data such as those from the Brazil Margin. Moreover, we have not included other uncertainties such as changes in tidal mixing, which may impact the LGM ocean (Wilmes et al., 2019).

5. Conclusion

Using a global coupled circulation biogeochemical model that includes the cycles of δ^{13} C and radiocarbon we have produced a series of LGM simulations with a range of circulation and deep water mass configurations. We find that simulations that have a shallow LGM AMOC (between 2000 and 2500 m, compared with modern data-based inferences of \sim 3500 m (Talley et al., 2003) and 4400 m (Danabasoglu et al., 2014)), with various possible rates of transport (between 8 and 18 Sv) are equally well constrained by our two isotopes from global data compilations. This represents a 1500 – 2500 m shoaling of NADW in the LGM, compared with previous estimates of ~ 500 m from a solution subject to a set of complementary constraints that included carbon isotopes (Gebbie, 2014). Locations where coring sites permit the reconstruction of high vertical resolution δ^{13} C profiles could be used to constrain the

LGM AMOC in a more detailed way, and appear to point at an intermediate AMOC strength during the LGM (11 - 18 Sv). More such locations are needed in order to increase the confidence of these estimates. LGM global radiocarbon age is shown to be highly correlated with SO surface reservoir age, which decreases with AMOC depth due to less sinking of dense waters. However, it is weakly affected by AMOC strength, contrary to past conjectures of a link between deep water mass transport and ventilation ages. The high anti-correlation that we find when comparing $\delta^{13}C$ and radiocarbon age changes between simulations suggest that these two tracers do not behave independently upon variations in deep ocean circulation. Our results seem to confirm previous analyses that also suggested a shallow glacial AMOC, but at the same time illustrate the inadequacy of global compilations of carbon isotopes alone to constrain AMOC transport rates well, calling for other paleo-tracers of physical ocean processes to be included in climate models.

Declaration of competing interest

The authors declare that they have no known competing financial interests or personal relationships that could have appeared to influence the work reported in this paper.

Acknowledgements

IM acknowledges funding from Conicet, Argentina, and NSF's Marine Geology and Geophysics and Chemical Oceanography Program (grants 1634719 and 1924215), USA. This work is a product of the Ocean Circulation and Carbon Cycling (OC3) project, funded by the Past Global Changes (PAGES) program. We want to thank David Lund for his help in providing the Brazil Margin data.

Appendix A. Supplementary data

Supplementary data to this article can be found online at https://doi.org/10.1016/j.quascirev.2021.106844.

Data availability

Model output is available upon request to the authors.

Author statement

Drs. Juan Muglia and Andreas Schmittner confirm that the work is original and has not been published or is in consideration for publication elsewhere. Both authors made substantial contributions to the manuscript. Dr. Juan Muglia ran the computer simulations. Both authors analyzed the results and wrote the manuscript. All authors approve the final version of the manuscript.

References

Adkins, J.F., 2013. The role of deep ocean circulation in setting glacial climates. Paleoceanography 28, 539–561. Adkins, J.F., Boyle, E.A., 1997. Changing atmospheric δ14c and the record of deep

water paleoventilation ages. Paleoceanography 12, 337-344.

Adkins, J.F., McIntyre, K., Schrag, D.P., 2002. The salinity, temperature, and δ180 of the glacial deep ocean. Science 298, 1769-1773.

Braconnot, P., Harrison, S.P., Kageyama, M., Bartlein, P.J., Masson-Delmotte, V., Abe-Ouchi, A., Otto-Bliesner, B., Zhao, Y., 2012. Evaluation of climate models using palaeoclimatic data. Nat. Clim. Change 2, 417.

Broecker, W., Clark, E., Barker, S., Hajdas, I., Bonani, G., Moreno, E., 2007. Radiocarbon age of late glacial deep water from the equatorial pacific. Paleoceanography 22.

Broecker, W.S., Peng, T.H., Trumbore, S., Bonani, G., Wolfli, W., 1990. The distribution of radiocarbon in the glacial ocean. Global Biogeochem. Cycles 4, 103-117.

Buizert, C., Schmittner, A., 2015. Southern Ocean control of glacial amoc stability

- and dansgaard-oeschger interstadial duration. Paleoceanography 30, 1595–1612
- Burke, A., Stewart, A.L., Adkins, J.F., Ferrari, R., Jansen, M.F., Thompson, A.F., 2015. The glacial mid-depth radiocarbon bulge and its implications for the overturning circulation. Paleoceanography 30, 1021–1039.
- Butzin, M., Köhler, P., Lohmann, G., 2017. Marine radiocarbon reservoir age simulations for the past 50,000 years. Geophys. Res. Lett. 44, 8473–8480.
- Campin, J.M., Fichefet, T., Duplessy, J.C., 1999. Problems with using radiocarbon to infer ocean ventilation rates for past and present climates. Earth Planet Sci. Lett. 165, 17–24.
- Cliff, E., Khatiwala, S., Schmittner, A., 2021. Glacial deep ocean deoxygenation driven by biologically mediated air—sea disequilibrium. Nat. Geosci. 1—8.
- Curry, W.B., Oppo, D.W., 2005. Glacial water mass geometry and the distribution of δ13C of ΣCO2 in the western Atlantic Ocean. Paleoceanography 20.
- Danabasoglu, G., Yeager, S.G., Bailey, D., Behrens, E., Bentsen, M., Bi, D., Biastoch, A., Böning, C., Bozec, A., Canuto, V.M., et al., 2014. North atlantic simulations in coordinated ocean-ice reference experiments phase ii (core-ii). part i: mean states. Ocean Model, 73, 76–107.
- Davies-Walczak, M., Mix, A.C., Stoner, J.S., Southon, J., Cheseby, M., Xuan, C., 2014. Late glacial to holocene radiocarbon constraints on north Pacific intermediate water ventilation and deglacial atmospheric CO2 sources. Earth Planet Sci. Lett. 397, 57–66.
- Duplessy, J., Shackleton, N., Fairbanks, R., Labeyrie, L., Oppo, D., Kallel, N., 1988. Deepwater source variations during the last climatic cycle and their impact on the global deepwater circulation. Paleoceanography 3, 343–360.
- Ferrari, R., Jansen, M.F., Adkins, J.F., Burke, A., Stewart, A.L., Thompson, A.F., 2014. Antarctic sea ice control on ocean circulation in present and glacial climates. Proc. Natl. Acad. Sci. Unit. States Am. 111, 8753–8758.
- Fyke, J., Sergienko, O., Löfverström, M., Price, S., Lenaerts, J.T., 2018. An overview of interactions and feedbacks between ice sheets and the Earth system. Rev. Geophys. 56, 361–408.
- Gebbie, G., 2014. How much did glacial north Atlantic water shoal? Paleoceanography 29, 190–209.
- Gu, S., Liu, Z., Oppo, D.W., Lynch-Stieglitz, J., Jahn, A., Zhang, J., Wu, L., 2020. Assessing the potential capability of reconstructing glacial Atlantic water masses and AMOC using multiple proxies in CESM. Earth Planet Sci. Lett. 541, 116294.
- Heinze, C., Maier-Reimer, E., Winn, K., 1991. Glacial pCO2 reduction by the world ocean: experiments with the hamburg carbon cycle model. Paleoceanography 6, 395–430.
- Hillenbrand, C.D., Cortese, G., 2006. Polar stratification: a critical view from the southern ocean. Palaeogeogr. Palaeoclimatol. Palaeoecol. 242, 240–252.
- Hoffman, J., Lund, D., 2012. Refining the stable isotope budget for Antarctic Bottom Water: new foraminiferal data from the abyssal southwest Atlantic. Paleoceanography 27.
- Hofmann, M., Rahmstorf, S., 2009. On the stability of the Atlantic meridional overturning circulation. Proc. Natl. Acad. Sci. Unit. States Am. 106, 20584–20589.
- Huybers, P., Gebbie, G., Marchal, O., 2007. Can paleoceanographic tracers constrain meridional circulation rates? J. Phys. Oceanogr. 37, 394–407.
- Insua, T.L., Spivack, A.J., Graham, D., D'Hondt, S., Moran, K., 2014. Reconstruction of Pacific ocean bottom water salinity during the last glacial maximum. Geophys. Res. Lett. 41, 2914–2920.
- Jaccard, S.L., Hayes, C.T., Martinez-Garcia, A., Hodell, D.A., Anderson, R.F., Sigman, D.M., Haug, G., 2013. Two modes of change in southern ocean productivity over the past million years. Science 339, 1419–1423.
- Kageyama, M., Albani, S., Braconnot, P., Harrison, S.P., Hopcroft, P.O., Ivanovic, R.F., Lambert, F., Marti, O., Peltier, W.R., Peterschmitt, J.Y.e.a., 2017. The pmip4 contribution to cmip6—part 4: scientific objectives and experimental design of the pmip4-cmip6 Last Glacial Maximum experiments and pmip4 sensitivity experiments. Geosci. Model Dev. (GMD) 10, 4035.
- Kageyama, M., Harrison, S.P., Kapsch, M.L., Löfverström, M., Lora, J.M., Mikolajewicz, U., Sherriff-Tadano, S., Vadsaria, T., Abe-Ouchi, A., Bouttes, N., et al., 2020. The pmip4-cmip6 last glacial maximum experiments: preliminary results and comparison with the pmip3-cmip5 simulations. Clim. Past 1—37. https://doi.org/10.5194/cp-2019-169.
- Key, R.M., Kozyr, A., Sabine, C.L., Lee, K., Wanninkhof, R., Bullister, J.L., Feely, R.A., Millero, F.J., Mordy, C., Peng, T.H., 2004. A global ocean carbon climatology: results from global data analysis project (glodap). Global Biogeochem. Cycles 18.
- Khatiwala, S., Primeau, F., Holzer, M., 2012. Ventilation of the deep ocean constrained with tracer observations and implications for radiocarbon estimates of ideal mean age. Earth Planet Sci. Lett. 325, 116–125.
- Khatiwala, S., Schmittner, A., Muglia, J., 2019. Air-sea disequilibrium enhances ocean carbon storage during glacial periods. Science advances 5, eaaw4981.
- Kurahashi-Nakamura, T., Paul, A., Losch, M., 2017. Dynamical reconstruction of the global ocean state during the Last Glacial Maximum. Paleoceanography 32, 326–350.
- Kvale, K.F., Meissner, K., Keller, D., Eby, M., Schmittner, A., 2015. Explicit planktic calcifiers in the university of victoria earth system climate model, version 2.9. Atmos.-Ocean 53, 332–350.
- Levitus, S., Antonov, J., Baranova, O.K., Boyer, T., Coleman, C., Garcia, H., Grodsky, A., Johnson, D., Locarnini, R., Mishonov, A.V., et al., 2013. The world ocean database. Data Sci. J. 12, WDS229—WDS234.
- Lund, D., Tessin, A., Hoffman, J., Schmittner, A., 2015. Southwest Atlantic water mass evolution during the last deglaciation. Paleoceanography 30, 477–494.

- Lynch-Stieglitz, J., Curry, W.B., Slowey, N., 1999. Weaker Gulf Stream in the Florida straits during the last glacial maximum. Nature 402, 644–648.
- Marchal, O., Curry, W.B., 2008. On the abyssal circulation in the glacial atlantic. J. Phys. Oceanogr. 38, 2014–2037.
- Marcott, S.A., Bauska, T.K., Buizert, C., Steig, E.J., Rosen, J.L., Cuffey, K.M., Fudge, T., Severinghaus, J.P., Ahn, J., Kalk, M.L., McConnell, J.R., Sowers, T., Taylor, K.C., White, J.W.C., J, B.E., 2014. Centennial-scale changes in the global carbon cycle during the last deglaciation. Nature 514, 616–619.
- Marshall, J., Scott, J.R., Romanou, A., Kelley, M., Leboissetier, A., 2017. The dependence of the ocean's moc on mesoscale eddy diffusivities: a model study. Ocean Model. 111. 1—8.
- McCarthy, G., Smeed, D., Johns, W., Frajka-Williams, E., Moat, B., Rayner, D., Baringer, M., Meinen, C., Collins, J., Bryden, H., 2015. Measuring the Atlantic meridional overturning circulation at 26 n. Prog. Oceanogr. 130, 91–111. Meissner, K., Weaver, A., Matthews, H., Cox, P., 2003. The role of land surface dy-
- Meissner, K., Weaver, A., Matthews, H., Cox, P., 2003. The role of land surface dynamics in glacial inception: a study with the Uvic Earth System Model. Clim. Dynam. 21, 515–537.
- Menviel, L., Spence, P., Skinner, L., Tachikawa, K., Friedrich, T., Missiaen, L., Yu, J., 2020. Enhanced mid-depth southward transport in the northeast Atlantic at the Last Glacial Maximum despite a weaker amoc. Paleoceanography and Paleoclimatology 35, e2019PA003793.
- Menviel, L., Yu, J., Joos, F., Mouchet, A., Meissner, K., England, M., 2017. Poorly ventilated deep ocean at the Last Glacial Maximum inferred from carbon isotopes: a data-model comparison study. Paleoceanography 32, 2–17.
- Muglia, J., Schmittner, A., 2015. Glacial Atlantic overturning increased by wind stress in climate models. Geophys. Res. Lett. 42, 9862–9868.
- Muglia, J., Skinner, L.C., Schmittner, A., 2018. Weak overturning circulation and high Southern Ocean nutrient utilization maximized glacial ocean carbon. Earth Planet Sci. Lett. 496, 47–56.
- Muglia, J., Somes, C.J., Nickelsen, L., Schmittner, A., 2017. Combined effects of atmospheric and seafloor iron fluxes to the glacial ocean. Paleoceanography 32, 1204–1218.
- Nikurashin, M., Vallis, G., 2012. A theory of the interhemispheric meridional overturning circulation and associated stratification. J. Phys. Oceanogr. 42, 1652–1667.
- Peltier, W., Argus, D., Drummond, R., 2015. Space geodesy constrains ice age terminal deglaciation: the global ice-6g_c (vm5a) model. J. Geophys. Res.: Solid Earth 120, 450–487.
- Peterson, C.D., Lisiecki, L.E., Stern, J.V., 2014. Deglacial whole-ocean δ13c change estimated from 480 benthic foraminiferal records. Paleoceanography 29, 549–563.
- Sarnthein, M., Schneider, B., Grootes, P.M., 2013. Peak glacial 14C ventilation ages suggest major draw-down of carbon into the abyssal ocean. Clim. Past 9, 2595–2614.
- Sarnthein, M., Winn, K., Jung, S.J., Duplessy, J.C., Labeyrie, L., Erlenkeuser, H., Ganssen, G., 1994. Changes in east atlantic deepwater circulation over the last 30,000 years: eight time slice reconstructions. Paleoceanography 9, 209–267.
- Schlitzer, R., Anderson, R.F., Dodas, E.M., Lohan, M., Geibert, W., Tagliabue, A., Bowie, A., Jeandel, C., Maldonado, M.T., Landing, W.M., et al., 2018. The geotraces intermediate data product 2017. Chem. Geol. 493, 210–223.
- Schmittner, A., 2003. Southern ocean sea ice and radiocarbon ages of glacial bottom waters. Earth Planet Sci. Lett. 213, 53–62.
- Schmittner, A., Bostock, H.C., Cartapanis, O., Curry, W.B., Filipsson, H.L., Galbraith, E.D., Gottschalk, J., Herguera, J.C., Hoogakker, B., Jaccard, S., et al., 2017. Calibration of the carbon isotope composition (δ13C) of benthic foraminifera. Paleoceanography 32, 512–530.
- Schmittner, A., Brook, E.J., Ahn, J., 2007. Impact of the ocean's overturning circulation on atmospheric co2. Ocean Circulation: Mechanisms and Impacts-Past and Future Changes of Meridional Overturning 209–246.
- Schmittner, A., Egbert, G., 2013. An improved parameterization of tidal mixing for ocean models. Geosci. Model Dev. (GMD) 6, 4475–4509.
- Schmittner, A., Gruber, N., Mix, A., Key, R., Tagliabue, A., Westberry, T., 2013. Biology and air—sea gas exchange controls on the distribution of carbon isotope ratios (δ 13 c) in the ocean. Biogeosciences 10, 5793—5816.
- Schmittner, A., Somes, C.J., 2016. Complementary constraints from carbon (13c) and nitrogen (15n) isotopes on the glacial ocean's soft-tissue biological pump. Paleoceanography 31, 669–693.
- Sigman, D.M., Boyle, E.A., 2000. Glacial/interglacial variations in atmospheric carbon dioxide. Nature 407, 859–869.
- Sigman, D.M., De Boer, A.M., Haug, G.H., 2007. Antarctic stratification, atmospheric water vapor, and heinrich events: a hypothesis for late pleistocene deglaciations. Ocean Circulation: Mechanisms and Impacts-Past and Future Changes of Meridional Overturning 335–349.
- Sigman, D.M., Hain, M.P., Haug, G.H., 2010. The polar ocean and glacial cycles in atmospheric CO2 concentration. Nature 466, 47–55.
- Sikes, E.L., Elmore, A.C., Allen, K.A., Cook, M.S., Guilderson, T.P., 2016. Glacial water mass structure and rapid δ18O and δ13C changes during the last glacial termination in the Southwest Pacific. Earth Planet Sci. Lett. 456, 87–97.
- Skinner, L., Primeau, F., Freeman, E., de la Fuente, M., Goodwin, P., Gottschalk, J., Huang, E., McCave, I., Noble, T., Scrivner, A., 2017. Radiocarbon constraints on the glacial ocean circulation and its impact on atmospheric co 2. Nat. Commun. 8, 1–10.
- Somes, C.J., Schmittner, A., Muglia, J., Oschlies, A., 2017. A three-dimensional model of the marine nitrogen cycle during the Last Glacial Maximum constrained by sedimentary isotopes. Frontiers in Marine Science 4, 108.

- Sun, S., Eisenman, I., Zanna, L., Stewart, A.L., 2020. Surface constraints on the depth of the atlantic meridional overturning circulation: southern ocean versus north atlantic. J. Clim. 33, 3125–3149.
- Tagliabue, A., Bopp, L., Roche, D., Bouttes, N., Dutay, J.C., Alkama, R., Kageyama, M., Michel, E., Paillard, D., 2009. Quantifying the roles of ocean circulation and biogeochemistry in governing ocean carbon-13 and atmospheric carbon dioxide at the Last Glacial Maximum. Clim. Past 5, 695—706.
- Talley, L.D., Reid, J.L., Robbins, P.E., 2003. Data-based meridional overturning streamfunctions for the global ocean. J. Clim. 16, 3213–3226.
- Tessin, A., Lund, D., 2013. Isotopically depleted carbon in the mid-depth South
- Atlantic during the last deglaciation. Paleoceanography 28, 296–306. Toggweiler, J.R., Russell, J.L., Carson, S.R., 2006. Midlatitude westerlies, atmospheric
- Toggweiler, J.R., Russell, J.L., Carson, S.R., 2006. Midlatitude westerlies, atmospheric CO2, and climate change during the ice ages. Paleoceanography 21.

 Weaver, A.J., Eby, M., Wiebe, E.C., Bitz, C.M., Duffy, P.B., Ewen, T.L., Fanning, A.F.,
- Weaver, A.J., Eby, M., Wiebe, E.C., Bitz, C.M., Duffy, P.B., Ewen, T.L., Fanning, A.F., Holland, M.M., MacFadyen, A., Matthews, H.D.e.a., 2001. The UVic Earth System Climate model: model description, climatology, and applications to past, present and future climates. Atmos.-Ocean 39, 361–428.
- Wilmes, S.B., Schmittner, A., Green, J., 2019. Glacial ice sheet extent effects on modeled tidal mixing and the global overturning circulation. Paleoceanography and Paleoclimatology 34, 1437–1454.